Running title: An endocytic myosin-1 generates power

Power generation by a myosin-1 essential for endocytosis: implications for biological mechanism

Ross TA Pedersen[1, 3, 4], Aaron Snoberger[2, 4], Serapion Pyrpassopoulos[2], Daniel Safer[2], David G Drubin[1*], E Michael Ostap[2*]

[1]Department of Molecular and Cell Biology, University of California, Berkeley, Berkeley, CA 94720

[2]Pennsylvania Muscle Institute, Perelman School of Medicine, University of Pennsylvania, Philadelphia, PA 19104

[3]Present address: Department of Embryology, Carnegie Institution for Science, Baltimore, MD 21218

[4]Equal Contribution

*Correspondence: drubin@berkeley.edu, ostap@mail.med.upenn.edu

Summary

Pedersen, Snoberger et al. measure the force-sensitivity of the yeast endocytic the myosin-1 called Myo5 and find that it is more likely to generate power than to serve as a force-sensitive anchor in cells. Implications for Myo5's role in clathrin-mediated endocytosis are discussed.

Abstract

Myosins are required for clathrin-mediated endocytosis, but their precise molecular roles in this process are not known. This is, in part, because the biophysical properties of the relevant motors have not been investigated. Myosins have diverse mechanochemical activities, ranging from powerful contractility against mechanical loads to force-sensitive anchoring. To better understand the essential molecular contribution of myosin to endocytosis, we studied the in vitro force-dependent kinetics of the *Saccharomyces cerevisiae* endocytic type I myosin called Myo5, a motor whose role in clathrin-mediated endocytosis has been meticulously studied in vivo. We report that Myo5 is a low-duty-ratio motor that is activated ~10-fold by phosphorylation, and that its working stroke and actin-detachment kinetics are relatively force-insensitive. Strikingly, the in vitro mechanochemistry of Myo5 is more like that of cardiac myosin than like that of slow anchoring myosin-1s found on endosomal membranes. We therefore propose that Myo5 generates power to augment actin assembly-based forces during endocytosis in cells.

Introduction

During clathrin-mediated endocytosis (CME), the plasma membrane invaginates and undergoes scission to become a cytoplasmic vesicle. Coat proteins like clathrin can deform membranes under low tension (Dannhauser and Ungewickell, 2012; Busch et al., 2015; Cail et al., 2022), but when membrane bending is resisted by membrane tension (Hassinger et al., 2017), the actin cytoskeleton drives plasma membrane invagination (Boulant et al., 2011; Kaplan et al., 2022). In yeasts, including *Saccharomyces cerevisiae* and *Schizosaccharomyces pombe*, turgor pressure opposes plasma membrane invagination, so actin is required at every CME site (Aghamohammadzadeh and Ayscough, 2009; Basu et al., 2013).

The actin cytoskeleton can produce pushing and pulling force, both of which are required for CME in *S. cerevisiae* (Sun et al., 2006). When actin filament ends grow against a surface, they push the surface forward (Mogilner and Oster, 1996, 2003). During CME, actin filaments, bound by coat proteins, grow against the plasma membrane at the base the CME site, driving invagination (Picco et al., 2015; Kaksonen et al., 2005, 2003; Skruzny et al., 2012, Fig. 1). Modeling of the homologous CME machinery in mammalian cells has demonstrated that such actin networks generate sufficient power for CME (Akamatsu et al., 2020), but whether actin assembly alone can overcome turgor pressure in yeast cells is under debate (Nickaeen et al., 2019; Carlsson, 2018).

Additional power may be provided by myosins, which generate tension on actin filaments. The myosins critical for CME, Myo3 and Myo5 in budding yeast, and Myo1e in vertebrates, are type I myosins (Geli and Riezman, 1996; Cheng et al., 2012; Krendel et al.,

2007). Some type I myosins are well-suited to generate power – i.e., they carry out mechanical work per unit time by consuming ATP to execute a power stroke. Other type I myosins are ideally suited to serve as force-sensitive anchors – their ATPase cycle is easily arrested by resistance, locking them in a state that maintains tension without completing the ATPase cycle or powering movement (Greenberg and Ostap, 2013). The possible roles of type I myosins in CME depend on whether endocytic myosins are power generators or force-sensitive anchors.

If endocytic type I myosins are acutely force-sensitive, they might organize the actin filaments of the endocytic actin network, while if they are less force sensitive, they could power plasma membrane invagination (Evangelista et al., 2000, Fig. 1). Myosin-1 motors form a ring at the base of CME sites, where the invaginated membrane meets the plasma membrane (Mund et al., 2018, Fig. 1). Yeast type I myosins serve at least one organizational function as a membrane anchor for the actin assembly machinery, a function associated with the non-motor tail of the molecules (Lewellyn et al., 2015), but motor activity is required in addition to membrane anchorage (Pedersen and Drubin, 2019). If endocytic myosin-1s are force sensitive anchors, they may serve a further organizational role by holding growing filaments in an optimal orientation for force generation (Fig. 1, left). If the myosins are power-generating motors, they may pull actin filament ends away from the plasma membrane, deepening the plasma membrane invagination and creating space for monomer addition and filament elongation (Fig. 1, right), a model supported by the observation that the actin assembly rate at CME sites depends on type I myosin motors in a dose-dependent manner (Manenschijn et al., 2019).

To distinguish between these possibilities, we measured the force sensitivity of the endocytic myosin Myo5 (not to be confused with the vertebrate type V myosin). Myo5 is insensitive to resistive force compared to related myosins. We therefore propose that Myo5 actively powers CME. Because actin and myosin collaborate in a variety of membrane remodeling processes, we expect that these results will be instructive beyond CME.

Results and Discussion

Heavy Chain Phosphorylation Activates Myo5 ATPase Activity

To determine how force sensitive Myo5 is, we first needed to measure its unloaded kinetics. We purified a Myo5 construct containing the motor and lever domains from *S. cerevisiae* (Fig. 2A). Because phosphorylation of Myo5 at the TEDS site is required for most CME events and is thought to regulate Myo5's motor activity (Grosshans et al., 2006; Sun et al., 2006; Bement and Mooseker, 1995), we purified a phosphorylated version and an unphosphorylated version of the protein separately (See Materials and methods). p21 activated kinase was used to phosphorylate the myosin at the TEDS site (S357), as determined by control experiments with an S357A mutant (Fig. S1). The phosphorylation state of preparations was judged to be uniform when ATP-induced actoMyo5 dissociation transients were well fit by single exponential functions (see below). The yeast light chain for Myo5, calmodulin (Cmd1, Geli et al., 1998) was purified from *E. coli* and included in excess in all experiments (Fig. 2A).

We measured the steady-state actin-activated ATPase activities of phosphorylated and unphosphorylated Myo5 using the NADH-coupled assay (De La Cruz and Ostap, 2009) in the presence of 0 - 80 μM phalloidin-stabilized actin. Unphosphorylated Myo5 ATPase activity was largely insensitive to actin: the ATPase rate for at 0 μM actin was 0.14 s^{-1}, while the maximum ATPase rate measured was 0.39 s^{-1} at 40 μM actin. (Fig. 2B). Phosphorylation activated Myo5 ATPase activity by about 10-fold (Fig. 2B). The actin concentration dependence of the phosphorylated Myo5 ATPase rate (k_{obs}) was well fit by:

$$k_{obs} = v_o \frac{V_{max}[Actin]}{K_{ATPase}+[Actin]} \qquad \textbf{(Equation 1)}$$

From the fit, the actin concentration at half-maximum of the ATPase rate (K_{ATPase}) was determined to be 5.1 ± 0.88 μM, and the maximum ATPase rate (V_{max}) was found to be 3.3 ± 0.15 s^{-1} (Fig, 2B; Table 1).

ATP Binding and ADP Release are Non-Rate Limiting for Myo5 ATPase Activity

Resistive force impacts the rate of myosin detachment from actin, and two biochemical transitions, ADP release and subsequent ATP binding, determine the detachment rate. Therefore, we used stopped-flow kinetics to measure ADP release from (Fig. 2C, k_{+5}') and ATP binding to (Fig. 2C, K_1' and k_{+2}') actoMyo5.

We found that yeast Myo5 does not quench the fluorescence of actin labeled at cys-374 with pyrene iodoacetamide, which is the probe most used to measure actomyosin attachment and detachment (De La Cruz and Ostap, 2009). Thus, we measured actoMyo5 detachment by monitoring light scattering, which decreases as myosin unbinds actin.

To determine the rate constant for ATP binding, we mixed nucleotide-free actoMyo5 (100 nM) with varying concentrations of ATP and monitored 90° light scattering in the stopped flow instrument. Light scattering time courses followed single exponential functions (Fig 2D). For phosphorylated Myo5, the observed rates determined from the fits increased linearly with ATP concentration (Fig. 2E). At concentrations of > 1 mM ATP, the actomyosin complex dissociated within the response time of the instrument, precluding measurement. For unphosphorylated Myo5, the observed rates fit a rectangular hyperbola with increasing ATP concentration (Fig. 2E).

The mechanism was modeled as (De La Cruz and Ostap, 2009):

$$AM + ATP \underset{}{\overset{K_1'}{\rightleftharpoons}} AM(ATP) \overset{k_2'}{\longrightarrow} AM.ATP \overset{k_{diss}}{\longrightarrow} A + M.ATP, \quad \textbf{(Scheme 1)}$$

where K_1' is a rapid equilibrium binding step, k_2' is a rate-limiting isomerization to the AM.ATP state, and k_{diss} is the rapid actin dissociation step. The apparent second order rate constant for ATP binding to phosphorylated actoMyo5 was determined by a linear fit to the data ($K_1'k_2'$ = 0.39 ± 0.017 μm^{-1} s^{-1}). The unphosphorylated actoMyo5 data were fit by:

$$k_{obs} = \left[\frac{K_1'[ATP]}{1 + K_1'[ATP]}\right] k_2', \qquad \textbf{(Equation 2)}$$

and the maximum rate of isomerization (k_2' = 290 ± 24 s^{-1}) and ATP affinity (K_1' = 0.006 ± 0.0016 μM^{-1}) were determined. The apparent second-order rate constant for ATP binding ($K_1'k_2'$) was determined from a linear fit of the observed rates below 100 μM ATP to be 1.1 ± 0.28 μM^{-1} s^{-1} (Table 1).

The rate constant for ADP dissociation (k_{+5}') was measured by preincubating 100 μM ADP with 200 nM actoMyo5 and then rapidly mixing with 2.5 mM ATP as shown in **scheme 2**:

$$A.M.ADP \underset{}{\overset{k_5'}{\rightleftharpoons}} A.M + ATP \rightleftharpoons A.M(ATP) \longrightarrow A + M.ATP, \quad \textbf{(Scheme 2)}$$

When myosin active sites are saturated with ADP, the rate of ATP-induced dissociation of actomyosin is limited by ADP's slow dissociation. Light scattering transients were fitted by single exponential functions, yielding rates for ADP release for phosphorylated actoMyo5 (k_{+5}' = 74 ± 2.0s^{-1}) and for unphosphorylated actoMyo5 (k_{+5}' = 107 ± 5.9 s^{-1}) (Fig. 2F and Table 1). The signal-to-noise ratio of the fast light scattering transients is low, resulting in large uncertainties on these fits. However, these rates are substantially faster than the

steady-state ATPase values, but slower than the maximum rate of ATP-induced actomyosin dissociation. ADP release for actoMyo5 ADP is much faster than ADP release for vertebrate Myo1b and Myo1c (Greenberg et al., 2012; Lewis et al., 2006). It is more similar to the vertebrate endocytic myosin-1, Myo1e (El Mezgueldi et al., 2002). Because ADP release is rate limiting for detachment of Myo5 and Myo1e from actin, fast ADP release by these molecules mean that the unloaded actin-attachment lifetimes for endocytic type I myosins are < 15 ms. This property may make these motors particularly well-suited to function in dynamic actin networks like those at CME sites, where actin filaments elongate and "treadmill" into the cytoplasm (Kaksonen et al., 2003, 2005).

Actin gliding is dependent on Myo5 phosphorylation state

Our kinetic results suggest that both phosphorylated and unphosphorylated Myo5 have low duty ratios (i.e., the motor spends a small fraction of its ATPase cycle bound to actin). Since ADP release limits the rate of phosphorylated Myo5 detachment from actin at saturating ATP (k_{+5}' = 74 ± 2.0 s^{-1}) and since we have measured the overall ATPase rate (V_{max} = 3.3 ± 0.15 s^{-1}), we can estimate the duty ratio:

$$Duty\ Ratio = \frac{(\frac{1}{k'_5})}{(\frac{1}{Vmax})}, \qquad \textbf{(Equation 3)}$$

The calculated duty ratio of phosphorylated Myo5 is 0.045. Unphosphorylated Myo5 has a lower duty ratio (< 0.004).

To assess the effect of phosphorylation on Myo5 motility, we performed in vitro motility assays at 1 mM ATP. Motors were attached site-specifically to coverslips coated with anti-His_6 antibody. Coverslips were incubated with a range of concentrations of

phosphorylated and unphosphorylated Myo5, creating a titration series of surface densities. At low Myo5 surface densities (incubation with ≤ 30 nM phosphorylated Myo5, ≤ 150 nM unphosphorylated Myo5), actin filaments failed to bind the coverslip (Fig. 2G and movies S1 and S2). At higher concentrations, phosphorylated Myo5 moved actin filaments at velocities ranging from 720 ± 40 nm/s (100 nM phosphorylated Myo5) to 880 ± 90 nm/s (40 nM) (Fig. 2G and movie S1). These gliding velocities are considerably higher than those reported by Sun et al., 2006, possibly reflecting differences in the phosphorylation state of the purified Myo5 protein (see below) or differences in other motility assay conditions, such as light chain availability. Higher (> 5-fold) surface densities of unphosphorylated Myo5 were required to achieve smooth motility, but this motility occurred at a substantially slower speed, ~120 nm/s (Fig. 2G and movie S2). While it is possible that residual phosphorylated Myo5 in the unphosphorylated prep contributed to this motility, Sun et al., 2006 similarly reported that Myo5 harboring TEDS site mutations moved actin filaments much more slowly. The slower actin gliding speed for unphosphorylated myosin was unexpected given the similar rates of ADP release between phosphorylated and unphosphorylated Myo5 (Table 1). It is possible that the our kinetics experiments have not determined the rate limiting step for detachment, but it is more likely that motility of the unphosphorylated myosin is limited by the slow attachment rate of the motor (Stewart et al., 2021), as suggested by the slow actin-activated ATPase rate. The activation of Myo5 motility by phosphorylation could explain why fast, cargo-induced endocytosis, which involves rapid and dynamic actin turnover, requires phosphorylated Myo5, while slower constitutive endocytosis does not (Grosshans et al., 2006).

Myo5's working stroke comprises two substeps that are consistent with unloaded kinetic measurements

The kinetics of actin attachment durations and mechanics of single myosin molecules were measured using an optical trapping instrument that can detect sub-nanometer displacements with millisecond temporal resolution (Woody et al., 2018; Snoberger et al., 2021). We used the three-bead optical trapping geometry in which a biotinylated actin filament is held between two laser-trapped polystyrene beads coated with neutravidin, creating a bead-actin-bead dumbbell (Fig. 3A). Dumbbells were lowered onto pedestal beads that were sparsely coated with phosphorylated Myo5-His_9 bound to a surface-adsorbed anti-His_6 tag antibody. The positions of trapped beads were detected via quadrant photodiode detectors, and single actomyosin binding events were detected by the decrease in covariance of the positions of the two dumbbell beads (Fig. 3B-D).

Traces acquired at 1, 10, and 1000 μM ATP reveal displacements and drops in covariance during actomyosin binding events. Individual points from covariance traces were fit by double gaussian distributions, with the thresholds for event detection indicated as dotted gray lines in Fig. 3 B-D. Event durations decreased with increasing ATP concentrations (Fig. 3 B-D, blue lines).

The myosin-1 working stroke has been shown to occur in two discrete substeps, with the first substep occurring with actin-activated phosphate release, and the second occurring with ADP release (Jontes et al., 1995; Veigel et al., 1999, Fig. 3E). The substeps can be characterized in optical trapping assays by ensemble averaging single interactions (Veigel et al., 1999; Chen et al., 2012; Laakso et al., 2008), where the detected events are

aligned at their beginnings and forward-averaged in time (Fig 3F-H, left), or aligned at their ends and reverse-averaged in time (Fig 3F-H, right).

Ensemble averages of Myo5 interactions showed a two-step working stroke at the three ATP concentrations, but the step-size was most accurately resolved at 10 μM ATP (see Materials and methods). In this condition, an initial substep of 4.8 nm was followed by a second substep of 0.2 nm (Fig. 3G). We determined the lifetimes of the substeps by fitting the ensemble averages with single exponential functions. At 1 μM ATP (Fig. 3F, left trace), the measured rate (> 30 s^{-1}) of the time-forward average was limited by the covariance smoothing window, but at 10 and 1000 μM ATP (Fig. 3 G-H, left traces), the rates were 49 ± 1.6 and 50 ± 0.2 s^{-1}, respectively (Fig. 3K) which are similar to the measured ADP release rate (k_{+5}', 74 ± 2.0 s^{-1}, Table 1) supporting the model that the transition from state-1 to state-2 accompanies ADP release.

The kinetics of time-reversed averages reveal the lifetime of State 2 (Fig. 3F-H, right traces). Fitting single exponential functions to these traces reveals rates of 0.59 ± 0.003 and 7.34 ± 0.1 s^{-1} at 1 and 10 μM ATP, respectively (Fig. 3K). At 1000 μM ATP, the observed rate (> 187 s^{-1}) was limited by the size of the covariance smoothing window (5.25 ms; Fig. 3K). The observed rates at 1 and 10 μM ATP are consistent with the second order rate constant for ATP binding of 0.39 ± 0.017 $\mu M^{-1}s^{-1}$ measured by stopped-flow kinetics ($K_1'k_{+2}$', Table 1).

We determined the detachment rates of actomyosin events by plotting the cumulative frequency of individual attachment durations and fitting a single exponential function to the data by maximum likelihood estimation (Fig. 3I). Data from 1 and 10 μM ATP were well fit by single exponentials with rates of 0.88 and 6.87 s^{-1}, respectively (Fig. 3I,

Fig. 3K). These rates match well with the observed rate of ATP binding (Table 1), as well as the fits for the reverse ensemble averages, indicating that at sub-saturating ATP (1 and 10 μM), detachment is limited by ATP binding (Figure 3J, blue squares & gray diamonds, Fig. 3K). Data from 1000 μM ATP were best described as the sum of 2 exponentials, with the major rate of 67.8 s^{-1} comprising 92.1% of the total, and a minor rate of 11.6 s^{-1} comprising 7.9% of the total (Fig. 3I, Fig. 3K). The major rate is consistent with both the observed ADP release rate and the measured forward ensemble average rates, indicating that at saturating ATP, ADP release limits detachment of actomyosin interactions (Fig. 3J**,** blue square and black diamond, Fig. 3K).

Myo5 is a relatively force-insensitive motor

To elucidate the force sensitivity of Myo5, we measured how its actin detachment rate was affected by mechanical force opposing the power stroke using an isometric feedback system that maintained the actin filament near its initial position (Takagi et al., 2006). The initial force applied to Myo5 in this system depends in part on where along the actin filament Myo5 stochastically binds, so this approach allowed measurement of attachment durations at a range of resistive forces (Fig. 4A). Plotting attachment durations as a function of force revealed a general trend of longer attachment durations at higher resisting forces. At each interaction force, attachment durations are exponentially distributed and, as expected based on prior isometric feedback experiments, the data appear noisy when plotted this way (Fig. 4A). Converting these data to detachment rates by binning them by force at every ten points, averaging, and taking the inverse of the attachment duration more clearly reveals the trend (Fig. 4B).

The force dependence of the Myo5 detachment rate was fit by the Bell Equation:

$$k(F) = k_0 \cdot e^{\frac{-F \cdot d}{k_B \cdot T}} \quad \textbf{(Equation 4)}$$

where *k(F)* is the detachment rate at force *F*, k_0 is the detachment rate in the absence of load, *d* is the distance parameter (the distance to the force-dependent transition state and a measure of force sensitivity), k_B is Boltzmann's constant, and *T* is the temperature. Best fit parameters for k_0 and *d* were determined by maximum likelihood estimation of the unaveraged data from Fig. 4A, incorporating the instrument response time (15-30 ms, Woody et al., 2016). The estimated detachment rate in the absence of force is 67.6 s^{-1}, in close agreement with the measured detachment rate under low load conditions at 1000 μM (saturating) ATP (67.8 s^{-1}, Fig. 3K). The best fit value for the distance parameter, *d*, was 1.14 nm.

To put Myo5's force sensitivity in context, we re-plotted the function describing the force-dependent actin detachment rate of Myo5 alongside the same curves for vertebrate Myo1b, Myo1c, and β-cardiac myosin, which have previously been determined by the same experimental approach (Fig. 4C, Laakso et al., 2010; Greenberg et al., 2012; Woody et al., 2018). The mechanochemistry of Myo5 (*d* = 1.14 nm) is most like that of β-cardiac (muscle) myosin (*d* = 1.3 nm), suggesting that it is well-suited for generating power. The difference between Myo5 and acutely force-sensitive Myo1b, a tension-sensitive anchor myosin (*d* = 15 nm), is dramatic. From 0 to 2 pN of resistance, Myo1b attachment lifetimes slow from ~600 ms to ~45 s, resulting in negligible power generation (Fig. 4D). Over the same interval, Myo5 attachment lifetimes slow very modestly from ~15 ms to ~25 ms, allowing

it to generate considerable power (Fig. 4D). Thus, Myo5 is unlikely to act as a force-sensitive anchor in cells and is more likely to power movements against a resisting load.

Proposed function of type I myosin in clathrin-mediated endocytosis

Myo5 is one of the best-studied myosin-1 proteins in vivo. Quantitative live cell imaging and electron microscopy have revealed that it is recruited to CME sites simultaneously with initiation of actin assembly, where it concentrates at the base of the site as membrane invagination proceeds (Jonsdottir and Li, 2004; Idrissi et al., 2008). Although it has long been appreciated that the presence (Geli and Riezman, 1996; Goodson et al., 1996) and mechanochemical activity (Sun et al., 2006) of type-1 myosins are required for CME, the mechanistic contribution of motor activity to the dynamic actin network was unknown. When it was discovered that some type I myosins are acutely force sensitive (Laakso et al., 2008), it became apparent that these motors could have mechanochemical activities that range from force-dependent anchoring to power generation during CME. However, distinguishing among these possibilities has been difficult in cells. Mutant Myo5 molecules lacking the motor head or bearing mutations intended to lock the ATPase in low and high actin affinity states each block CME, results that do not reveal the mechanochemical role of Myo5 (Lewellyn et al., 2015; Idrissi et al., 2012). Perhaps the most informative finding in cells has been the observation that varying the number of type I myosins at CME sites results in differences in actin assembly rates (Manenschijn et al., 2019). However, because resistive load remodels growing branched actin networks in complex ways (Bieling et al., 2016), even this finding did not clearly differentiate between the possible roles for endocytic myosin-1s.

Here we have shown that Myo5's motor generates power rather than forming force-sensitive catch bonds. The overall ATPase rate of Myo5 is slow relative to other power-generating myosins, but its power stroke and detachment from actin are fast, and they slow only modestly under load (Fig. 4C). Myo5's relative force insensitivity means it generates steady power against resistance (Fig. 4D). Because Myo3 and Myo5 can each support CME in the absence of the other, we suspect that Myo3 is similarly force-insensitive. Given the structural and functional homology between Myo5 and vertebrate Myo1e, together with the close agreement of their unloaded kinetics (El Mezgueldi et al., 2002), we also predict the Myo1e generates biologically relevant power.

Our finding that Myo5's kinetics are relatively force insensitive lead us to interpret the previously described dose dependence of actin assembly on the number of myosin-1s at endocytic sites to mean that this motor moves actin filaments at CME sites to power plasma membrane invagination and create space for new monomers to assemble (Manenschijn et al., 2019, Fig. 1, right). On the order of 300 myosin molecules (Myo3 and Myo5 combined) are present at CME sites, mostly where the invaginating membrane meets the plasma membrane (Mund et al., 2018; Idrissi et al., 2008; Sun et al., 2019; Picco et al., 2015). A related myosin, Myo1c, also binds membranes and can generate and sustain sub-piconewton forces parallel to the plane of the membrane, and greater forces when moving actin filaments away from the membrane or when diffusion within the bilayer is impeded (Pyrpassopoulos et al., 2016). Myo5's diffusion is likely to be impeded by the many proteins at the base of CME sites, and it may move actin filaments at an angle to the membrane it is bound to. Actin subunits "treadmill" towards the cytoplasm in endocytic actin networks at ~50-100 nm/s (Kaksonen et al., 2005, 2003), so Myo5's motility rate of 700-900 nm/s (Fig.

2G), which we would expect resistance to slow only modestly, is fast enough to do work on the actin network as it assembles. We therefore expect that the myosins power membrane invagination and relive load to accelerate actin assembly during CME.

Type I myosins are involved in a variety of membrane reshaping events in cells, where they often interact with growing branched actin networks (Sokac et al., 2006; Almeida et al., 2011; Joensuu et al., 2014; Krendel et al., 2007; Cheng et al., 2012), but the relative contributions of myosin motor activity and actin assembly have rarely been resolved. Here, we demonstrated that a type I myosin critical for CME, a process well-known to be driven by actin assembly, generates power. Implication of endocytic type I myosin as a force-insensitive motor suggests that actin assembly and myosin power generation can be coordinated to do coherent work in membrane remodeling processes.

Materials and methods

Reagents, proteins, and buffers

ATP concentrations were determined spectrophotometrically after each experiment by absorbance at 259 nm, $\epsilon_{259} = 15{,}400\ M^{-1}cm^{-1}$. Rabbit skeletal muscle actin was prepared and gel filtered (Spudich and Watt, 1971). Actin concentrations were determined spectrophotometrically by absorbance at 290 nm, $\epsilon_{290} = 26{,}600\ M^{-1}cm^{-1}$. All actin was stabilized with one molar equivalent of phalloidin (Sigma). Steady state, transient, and single molecule experiments were performed at 20°C in KMg25 buffer (60 mM MOPS pH 7, 25 mM KCl, 1 mM EGTA, 1 mM $MgCl_2$, 1 mM DTT). Apyrase VII was obtained from Sigma. Purity and concentration of purified proteins were determined by comparing in-gel Coomassie blue staining to staining of known amounts of bovine serum albumin (Pierce).

Expression and Purification of Cmd1

The *S. cerevisiae* calmodulin gene *CMD1* was cloned from genomic DNA into a bacterial expression plasmid with a sequence encoding His_6-TEV situated at the 5' end to generate pDD2743. pDD2743 was transformed into Rosetta *E. coli*, optimized for expression (Novagen). A saturated overnight culture in LB (10 g/L Bacto tryptone, 5 g/L Bacto yeast extract, 10 g/L NaCl) was used to inoculate a 1 L culture in LB to OD_{600} = 0.1. Cells were grown to OD_{600} = 0.6-1, induced with 0.5 mM IPTG for 5 hours at 37°C, pelleted at 4,225 x g for 20 minutes at 4°C in a Sorvall SLA-3000 (fixed angle) rotor, washed with cold 20 mM HEPES pH 7.5, and repelleted at 2,250 x g for 10 minutes at 4°C in a Jouan CR3i (swinging bucket) centrifuge. Cell pellets were flash frozen in 45 mL lysis buffer (20 mM HEPES pH

7.5, 1 M KCl, 20 mM Imidazole). Upon thawing, cells were lysed by sonication, 2 mg DNase I (Roche) and triton X-100 to 1% were added, and the resulting lysate was incubated on ice for 30 minutes, then spun at 92,000 x g for 25 minutes in a Beckman Type 70 Ti rotor. The supernatant was loaded onto a 1 mL HisTrap HP column (GE healthcare) preequilibrated with binding buffer (20 mM HEPES pH 7.5, 500 mM KCl, 20 mM imidazole). The column was washed with 20 mL binding buffer, and Cmd1 was eluted using a 30 mL linear gradient from 0-100% elution buffer (20 mM HEPES pH 7.5, 500 mM KCl, 500 mM imidazole). Fractions containing Cmd1 were pooled, Cmd1 was cleaved from His_6 with TEV protease and dialyzed overnight at 4°C into low salt buffer (10 mM Tris pH 7, 25 mM NaCl, 2 mM $MgCl_2$, 5 mM DTT). Following dialysis, purified, cleaved Cmd1 was bound to a MonoQ column and eluted using a 10 mL linear gradient from 0-70% high salt buffer (10 mM Tris pH 7, 1 M NaCl, 2 mM $MgCl_2$, 5 mM DTT). Fractions containing Cmd1 were pooled, dialyzed into KMg50 buffer (60 mM MOPS pH 7, 50 mM KCl, 1 mM $MgCl_2$, 1 mM EGTA, 1 mM DTT, 5% glycerol), and stored at -80°C.

Expression and Purification of Myo5

Myo5 was coexpressed with the myosin chaperone She4 in *S. cerevisiae.* The *MYO5* open reading frame (ORF) from *S. cerevisiae* was cloned from genomic DNA and truncated at Gly^{763}, generating a construct containing the motor domain and both Cmd1-binding IQ motifs of the lever arm. The *SHE4* ORF was cloned in its entirety from *S. cerevisiae* genomic DNA. Both ORFs were ligated into a 2µ expression plasmid with a partially defective *LEU2* gene (*leu2d*) to ensure high copy number, creating plasmid pDD2744 (parent vector described in Roy et al., 2011). The *MYO5* ORF was situated with a sequence encoding

AviTag-TEV-His_9 at the 3' end. Expression of the *MYO5* and *SHE4* ORFs was driven by a bidirectional Gal 1/10 promotor.

pDD2744 was transformed into D1074 yeast (Roy et al., 2011). Saturated overnight cultures in synthetic minimal medium (1.5 g/L Difacto yeast nitrogen base, 5 g/L ammonium sulfate, supplemented with 2% glucose 20 µg/mL adenine, L-histadine, L-methionine, and 30 µg/mL L-lysine) were used to inoculate 1.5 L cultures in the same media with raffinose substituted for glucose to OD_{600} = 0.1. After 18 hours of growth at 30°C, cultures were induced with 2% galactose, Bacto yeast extract was added to 10 g/L, and Bacto peptone to 20 g/L. After 8 hours of expression, the cells were harvested at 4,225 x g for 20 minutes at 4°C in a Sorvall SLA-3000 rotor, washed with 25 mL cold Milli-Q water, repelleted at 2,250 x g for 10 minutes at 4°C in a Jouan CR3i centrifuge, resuspended in 0.2 volumes of cold Milli-Q water, and drop frozen into liquid nitrogen. Lysis was achieved through cryomilling (10 cycles of 3 minutes grinding with one minute cooldown) in the large vials of a 6870 freezer/mill (SPEX Sample Prep).

Cell powders were thawed in binding buffer (10 mM Tris pH 7, 500 mM NaCl, 4 mM $MgCl_2$, 2 mM ATP, 20 mM imidazole, 5 mM DTT) supplemented with 1 mM PMSF, 1 x cOmplete protease inhibitor cocktail without EDTA (Roche), and 1 µM Cmd1. For purification of phosphorylated Myo5, 1 µg Pak1 (Sigma, Brzeska et al., 1997, Fig. S1) was included in the lysis buffer and 10 mM β-glycerophosphate, 5 mM sodium pyrophosphate, and 50 mM sodium fluoride were included in all purification buffers. For purification of unphosphorylated Myo5, 4000 units lambda phosphatase (NEB) and 1 mM $MnCl_2$ were included in the lysis buffer. The lysate was then spun at 345,000 x g for 10 minutes at 4°C in a Beckman TLA100.3 rotor, filtered through a 0.22 µm filter, and loaded onto a 1 mL

HisTrap HP column. The column was washed with wash buffer (Binding buffer with only 200 mM NaCl), and Myo5 was eluted using a 20 mL linear gradient from 0-100% elution buffer (wash buffer with 1 M imidazole).

Fractions containing Myo5 were pooled and supplemented with Cmd1 to 1 μM. For unphosphorylated Myo5 purification, a further 20,000 units lambda phosphatase were added along with $MnCl_2$ to 1 mM and the fractions were incubated at 30°C for 30 minutes. Purified protein was dialyzed through a 3.5 KDa MWCO membrane into 1 L storage buffer (KMg50 with 50% glycerol) overnight at 4°C and again into 500 mL of the same buffer for 2 hours at 4°C, then stored at -20°C.

Kinetic measurements

Kinetic experiments were conducted using an Applied Photophysics (Surrey, UK) SX.18 MV stopped-flow apparatus. To monitor light scattering at 90˚, 450 nm excitation light was used with a 400 nm emission filter. Experimental transients were fit by single exponentials using the software provided with the stopped flow apparatus. 1-7 traces were averaged together to generate each data point. Steady state actin-activated ATPase activity was measured using the NADH enzyme-linked assay (De La Cruz and Ostap, 2009). NADH loss was monitored by absorbance at 340 nm (ϵ_{340} = 6,220 $M^{-1}cm^{-1}$). ATP-induced dissociation of actoMyo5 was measured and analyzed as described (De La Cruz and Ostap, 2009). 0.04 units/mL apyrase was added to solutions of actoMyo5 before mixing to remove contaminating ADP and ATP. Unphosphorylated actoMyo5 required prolonged treatment with apyrase to achieve sufficient signal, presumably because a larger fraction of the

435 population was bound to ATP left over from purification and because the actin-activated
436 ATPase rate of unphosphorylated Myo5 is slow. Concentrations reported are post mixing.
437
438 **Motility assays**
439 Motility assays were performed essentially as described (Lin et al., 2005). Myo5 was
440 adhered to nitrocellulose coated coverslips via 20 µg anti His_6 antibody (Sigma) blocked
441 with 2 mg/mL casein. Blocking coverslips with bovine serum albumin (BSA) led to inferior
442 gliding. Motility was recorded in the presence of 1 mM ATP and 5 µM Cmd1. The rate of
443 actin filament gliding was determined using the manual tracking plugin in Fiji.
444
445 **Optical trapping**
446 Flow chambers for optical trapping were constructed with double-sided tape and vacuum
447 grease as previously described (Snoberger et al., 2021; Greenberg et al., 2017). Briefly, the
448 coverslip was coated with a 0.1% mixture of nitrocellulose and 2.47 µm diameter silica
449 beads. Coverslips were dried at least 30 minutes and were used within 24 hours of
450 preparation. To define the walls of the flow cell, 2 strips of double-sided tape were placed
451 ~5 mm apart, a 1 mm thick glass slide was placed on top, and carefully sealed with vacuum
452 grease after addition of final buffer.
453 Trapping buffer (KMg25 with 1 mM DTT freshly added) was used for all trapping
454 assays. A 100x stock of glucose oxidase + catalase (GOC) was freshly prepared by
455 centrifuging catalase (Sigma, > 30000 $U \cdot mL^{-1}$) at 15,000 x g for 1 minute, and adding 2 µl of
456 catalase supernatant to 20 µL of 19.1 U/µL glucose oxidase (Sigma).

0.01 mg/mL anti-His_6 antibody (Sigma) was flowed in the chamber and incubated between 30 seconds and 3 minutes, then immediately blocked with two, 3-minute incubations of 1 - 2 mg/mL BSA. Stocks of phosphorylated His_9-tagged Myo5 were diluted to 1 nM in trapping buffer with 300 mM added KCl and incubated in the flow cell for 2 minutes. The number of myosins bound to the surface was limited by the surface concentration of anti-His_6 antibody, and the incubation time of anti-His_6 antibody was adjusted daily between 30 seconds and 3 minutes such that 1 of 3 - 5 pedestals tested showed clear myosin interactions with the actin dumbbell.

Following incubation with Myo5, a second blocking step with two, 3-minute incubations of 1 - 2 mg/mL BSA was performed. Final buffer added to the flow cell contained trapping buffer with indicated amount of ATP, 1 µL of GOC added immediately prior to addition to chamber, and 0.1 - 0.25 nM rabbit skeletal muscle actin polymerized with 15% biotinylated actin (Cytoskeleton) stabilized by rhodamine-phalloidin (Sigma) at a 1.1-1.2 molar ratio with G-actin concentration. Neutravidin-coated beads were prepared by incubating 0.4 ng of 0.8 µm diameter polystyrene beads (Polysciences) and coated with 5 mg/mL neutravidin (Thermo Fisher). 3 µL of neutravidin-coated beads were added to one side of the chamber prior to sealing. All trapping data were acquired within 90 minutes of addition of the final buffer to the chamber.

Optical trapping experiments were performed at room temperature (20 ± 1 °C) using a dual beam 1064 nm trapping laser as described in (Woody et al., 2018, 2017). A single laser beam was split into 2 beams using polarizing beam splitters and steered into a 60x water immersion objective (Nikon). Laser light was projected through an oil immersion condenser and into quadrant photodiodes (JQ-50P, Electro Optical Components,

Inc.), each of which were conjugate to the back focal plane of the objective. Direct force detection from the quadrant photodiodes was achieved using a custom-built high-voltage reverse bias and an amplifier. Data acquisition, beam position control output, and isometric feedback calculations were controlled with custom-built virtual instruments (Labview, Matlab).

Individual 0.8 μm diameter neutravidin-coated bead were caught in the two traps and held approximately 5 μm apart. Trap stiffnesses were adjusted to 0.05 – 0.1 pN/nm for each trap. A biotinylated actin filament visualized by rhodamine phalloidin was bound to the two trapped beads, creating a bead-actin-bead dumbbell. The dumbbell was pretensioned (3-5 pN) by steering one beam using a piezo controlled mirror conjugate to the back focal plane of the objective, and the surface of pedestal beads were probed for myosins. Putative myosin interactions were detected via drops in variance of the two beads, and the 3-dimensional position of the dumbbell relative to the myosin was refined further by maximizing the rate and size of the observed power stroke deflections. Every 30-60 s, the dumbbell was moved axially along the actin filament in ~6 nm steps between trace acquisition to ensure even accessibility of actin-attachment target zones. Stage drift was corrected via a feedback system using a nano-positioning stage and imaging the position of the pedestal bead with nm precision (Woody et al., 2017). In experiments using 1 μM ATP, due to the longer actomyosin interactions, stage drift was still observed even with the stage feedback engaged, leading to a presumed underestimation of the displacement size. All data were acquired at a sampling rate of 250 kHz.

Isometric optical clamping experiments were performed as described in (Woody et al., 2018; Takagi et al., 2006) using a digital feedback loop and a 1-D electro-optical

503 deflector (EOD, LTA4-Crystal, Conoptics) to steer the beam position using input from a high
504 voltage source (Conoptics, Model 420 Amplifier). Briefly, the position of one bead (the
505 "transducer" bead) was maintained at a constant position by adjusting the position of the
506 other bead (referred to as the "motor" bead) during actomyosin interactions. The response
507 time of the feedback loop during actomyosin interactions was ~15-30 ms.
508
509 **Optical trap data analysis**
510 Actomyosin interactions for non-isometric optical clamping experiments were detected
511 using the single-molecule computational tool SPASM (Software for Precise Analysis of
512 Single Molecules , Blackwell et al., 2021), which uses a calculation of the dumbbell bead
513 covariances and a change-point algorithm. Data collected at 1000 μM ATP were analyzed at
514 250 kHz, while data collected at 1 and 10 μM ATP were downsampled to 2 kHz by
515 averaging every 125 points to enhance analysis speed. Events were detected by calculating
516 the covariance of the 2 beads using a smoothing window of 33.3, 15, and 5.25 ms and an
517 averaging window 60, 36, and 12 ms at 1, 10, and 1000 μM ATP, respectively. The
518 instrument deadtime was calculated to be 2 times the covariance averaging window. For
519 each 15 s trace, the detected covariance was plotted and fit to double gaussian
520 distributions, with the smaller mean gaussian corresponding to the actomyosin "bound"
521 portion and the larger mean gaussian corresponding to the "unbound" portion of events. A
522 putative event was defined as an event where the covariance starts above the unbound
523 peak mean, drops below the bound peak mean, and remains below the unbound peak mean
524 for at least the length of the instrument deadtime prior to returning back above unbound
525 peak mean. Event starts and ends were further refined using a changepoint algorithm as

526 described (Blackwell et al., 2021). Attachment durations and ensemble averages of single
527 events were determined using built-in features in the SPASM software. Exponential fits for
528 forward and reverse ensemble averages were performed in Origin 2019 graphing &
529 analysis software (OriginLab).

530 Events detected in isometric optical clamping experiments were detected as
531 described in (Takagi et al., 2006) using a zero crossing analysis via custom MATLAB scripts.
532 Briefly, when a myosin is actively engaged with the dumbbell, force is applied to the
533 transducer bead, a feedback loop is engaged and opposing force applied to the motor bead
534 until the position of the transducer bead is restored. Beginnings of events are defined at the
535 point at which the feedback signal increases from baseline in the motor bead and ends of
536 events are defined when the feedback signal decreases back below the baseline in the
537 motor bead.

538

539 **Online supplemental material**

540 Figure S1 shows the results of a kinase assay demonstrating that Pak1, used to in
541 purifications of phosphorylated Myo5, specifically phosphorylates Myo5 serine-357.

Acknowledgements

We thank M. Greenberg, E. Lewellyn, and A. Kunibe, each of whom played important roles at the inception of this study. We thank Y.E. Goldman for optical trap instrumentation. We thank M. Ferrin for helpful comments on the manuscript. This work was funded by National Institute of General Medical Sciences (NIGMS) grant R35 GM118149 to D.G.D and grant 5R37GM057247 to E.M.O. R.T.A.P. is currently funded by NIGMS F32 GM142145.

References

Aghamohammadzadeh, S., and K.R. Ayscough. 2009. Differential requirements for actin during yeast and mammalian endocytosis. *Nat. Cell Biol.* 11:1039–1042. doi:10.1038/ncb1918.

Akamatsu, M., R. Vasan, D. Serwas, M. Ferrin, P. Rangamani, and D.G. Drubin. 2020. Principles of self-organization and load adaptation by the actin cytoskeleton during clathrin-mediated endocytosis. *Elife*. 9:1–40. doi:10.7554/eLife.49840.

Almeida, C.G., A. Yamada, D. Tenza, D. Louvard, G. Raposo, and E. Coudrier. 2011. Myosin 1b promotes the formation of post-Golgi carriers by regulating actin assembly and membrane remodelling at the trans-Golgi network. *Nat. Cell Biol.* 13:779–789. doi:10.1038/ncb2262.

Basu, R., E.L. Munteanu, and F. Chang. 2013. Role of turgor pressure in endocytosis in fission yeast. *Mol. Biol. Cell*. 25:679–87. doi:10.1091/mbc.E13-10-0618.

Bement, W.M., and M.S. Mooseker. 1995. TEDS rule: A molecular rationale for differential regulation of myosins by phosphorylation of the heavy chain head. *Cell Motil. Cytoskeleton*. 31:87–92. doi:10.1002/cm.970310202.

Bieling, P., T. Li, J. Weichsel, R. Mcgorty, P. Jreij, B. Huang, D.A. Fletcher, and R.D. Mullins. 2016. Force Feedback Controls Motor Activity and Mechanical Properties of Self-Assembling Branched Actin Networks. *Cell*. 164:115–127. doi:10.1016/j.cell.2015.11.057.

Blackwell, T., W.T. Stump, S.R. Clippinger, and M.J. Greenberg. 2021. Computational Tool for Ensemble Averaging of Single-Molecule Data. *Biophys. J.* 120:10–20.

572 doi:10.1016/j.bpj.2020.10.047.

573 Boulant, S., C. Kural, J.-C. Zeeh, F. Ubelmann, and T. Kirchhausen. 2011. Actin dynamics
574 counteract membrane tension during clathrin-mediated endocytosis. *Nat. Cell Biol.*
575 13:1124–31. doi:10.1038/ncb2307.

576 Brzeska, H., U.G. Knaus, Z.Y. Wang, G.M. Bokoch, and E.D. Korn. 1997. p21-activated kinase
577 has substrate specificity similar to Acanthamoeba myosin I heavy chain kinase and
578 activates Acanthamoeba myosin I. *Proc. Natl. Acad. Sci. U. S. A.* 94:1092–1095.

579 Busch, D.J., J.R. Houser, C.C. Hayden, M.B. Sherman, E.M. Lafer, and J.C. Stachowiak. 2015.
580 Intrinsically disordered proteins drive membrane curvature. *Nat. Commun.* 6.
581 doi:10.1038/ncomms8875.

582 Cail, R.C., C.R. Shirazinejad, and D.G. Drubin. 2022. Induced nanoscale membrane curvature
583 bypasses the essential endocytic function of clathrin. *J. Cell Biol.* 221.
584 doi:10.1083/jcb.202109013.

585 Carlsson, A.E. 2018. Membrane bending by actin polymerization. *Curr. Opin. Cell Biol.* 50:1–
586 7. doi:10.1016/j.ceb.2017.11.007.

587 Chen, C., M.J. Greenberg, J.M. Laakso, E.M. Ostap, Y.E. Goldman, and H. Shuman. 2012.
588 Kinetic schemes for post-synchronized single molecule dynamics. *Biophys. J.* 102.
589 doi:10.1016/j.bpj.2012.01.054.

590 Cheng, J., A. Grassart, and D.G. Drubin. 2012. Myosin 1E coordinates actin assembly and
591 cargo trafficking during clathrin-mediated endocytosis. *Mol. Biol. Cell*. 23:2891–904.
592 doi:10.1091/mbc.E11-04-0383.

593 Dannhauser, P.N., and E.J. Ungewickell. 2012. Reconstitution of clathrin-coated bud and
594 vesicle formation with minimal components. *Nat. Cell Biol.* 14:634–639.

595 doi:10.1038/ncb2478.

596 Evangelista, M., B.M. Klebl, A.H. Yong, B.A. Webb, T. Leeuw, E. Leberer, M. Whiteway, D.Y.
597 Thomas, and C. Boone. 2000. A Role for Myosin-I in Actin Assembly through
598 Interactions with Vrp1p, Bee1p, and the Arp2/3 Complex. *J. Cell Biol.* 148:353–362.
599 doi:10.1083/jcb.148.2.353.

600 Geli, M.I., and H. Riezman. 1996. Role of Type I Myosins in Receptor-Mediated Endocytosis
601 in Yeast. *Science*. 272:533–535.

602 Geli, M.I., A. Wesp, and H. Riezman. 1998. Distinct functions of calmodulin are required for
603 the uptake step of receptor-mediated endocytosis in yeast: The type I myosin Myo5p is
604 one of the calmodulin targets. *EMBO J.* 17:635–647. doi:10.1093/emboj/17.3.635.

605 Goodson, H. V, B.L. Anderson, H.M. Warrick, L.A. Pon, and J.A. Spudich. 1996. Synthetic
606 lethality screen identifies a novel yeast myosin I gene (MYO5): myosin I proteins are
607 required for polarization of the actin cytoskeleton. *J. Cell Biol.* 133:1277–1291.
608 doi:10.1083/JCB.133.6.1277.

609 Greenberg, M.J., T. Lin, Y.E. Goldman, H. Shuman, and E.M. Ostap. 2012. Myosin IC generates
610 power over a range of loads via a new tension-sensing mechanism. *Proc. Natl. Acad.*
611 *Sci. U. S. A.* 109:E2433-40. doi:10.1073/pnas.1207811109.

612 Greenberg, M.J., and E.M. Ostap. 2013. Regulation and control of myosin-I by the motor and
613 light chain-binding domains. *Trends Cell Biol.* 23:81–9. doi:10.1016/j.tcb.2012.10.008.

614 Greenberg, M.J., H. Shuman, and E.M. Ostap. 2017. Measuring the Kinetic and Mechanical
615 Properties of Non-processive Myosins Using Optical Tweezers. *Methods Mol. Biol.*
616 1486:483–509. doi:10.1201/b22505.

617 Grosshans, B.L., H. Grötsch, D. Mukhopadhyay, I.M. Fernández, J. Pfannstiel, F.-Z. Idrissi, J.

618 Lechner, H. Riezman, and M.I. Geli. 2006. TEDS site phosphorylation of the yeast
619 myosins I is required for ligand-induced but not for constitutive endocytosis of the G
620 protein-coupled receptor Ste2p. *J. Biol. Chem.* 281:11104–14.
621 doi:10.1074/jbc.M508933200.
622 Hassinger, J.E., G. Oster, D.G. Drubin, and P. Rangamani. 2017. Design principles for robust
623 vesiculation in clathrin-mediated endocytosis. *Proc. Natl. Acad. Sci. U. S. A.* 114:E1118–
624 E1127. doi:10.1073/pnas.1617705114.
625 Idrissi, F.-Z., A. Blasco, A. Espinal, and M.I. Geli. 2012. Ultrastructural dynamics of proteins
626 involved in endocytic budding. *Proc. Natl. Acad. Sci. U. S. A.* 109:E2587–E2594.
627 doi:10.1073/pnas.1202789109.
628 Idrissi, F.Z., H. Grötsch, I.M. Fernández-Golbano, C. Presciatto-Baschong, H. Riezman, and
629 M.I. Geli. 2008. Distinct acto/myosin-I structures associate with endocytic profiles at
630 the plasma membrane. *J. Cell Biol.* 180:1219–1232. doi:10.1083/jcb.200708060.
631 Joensuu, M., I. Belevich, O. Rämö, I. Nevzorov, H. Vihinen, M. Puhka, T.M. Witkos, M. Lowe,
632 M.K. Vartiainen, and E. Jokitalo. 2014. ER sheet persistence is coupled to myosin 1c-
633 regulated dynamic actin filament arrays. *Mol. Biol. Cell*. 25:1111–1126.
634 doi:10.1091/mbc.E13-12-0712.
635 Jonsdottir, G. a., and R. Li. 2004. Dynamics of Yeast Myosin I: Evidence for a Possible Role in
636 Scission of Endocytic Vesicles. *Development*. 14:1604–1609. doi:10.1016/j.
637 Jontes, J.D., E.M. Wilson-Kubalek, and R.A. Milligan. 1995. A 32 degree tail swing in brush
638 border myosin I on ADP release. *Nature*. 378:751–753. doi:10.1038/378751a0.
639 Kaksonen, M., Y. Sun, and D.G. Drubin. 2003. A pathway for association of receptors,
640 adaptors, and actin during endocytic internalization. *Cell*. 115:475–87.

641 Kaksonen, M., C.P. Toret, and D.G. Drubin. 2005. A modular design for the clathrin- and
642 actin-mediated endocytosis machinery. *Cell*. 123:305–20.
643 doi:10.1016/j.cell.2005.09.024.
644 Kaplan, C., S.J. Kenny, X. Chen, J. Schöneberg, E. Sitarska, A. Diz-Muñoz, M. Akamatsu, K. Xu,
645 and D.G. Drubin. 2022. Load adaptation by endocytic actin networks. *Mol. Biol. Cell*. 33.
646 doi:10.1091/mbc.E21-11-0589.
647 Krendel, M., E.K. Osterweil, and M.S. Mooseker. 2007. Myosin 1E interacts with
648 synaptojanin-1 and dynamin and is involved in endocytosis. *FEBS Lett.* 581:644–50.
649 doi:10.1016/j.febslet.2007.01.021.
650 De La Cruz, E.M., and E.M. Ostap. 2009. Kinetic and Equilibrium Analysis of the Myosin
651 ATPase. *Methods Enzymol.* 455:157–192. doi:10.1016/S0076-6879(08)04206-7.
652 Laakso, J.M., J.H. Lewis, H. Shuman, and E.M. Ostap. 2008. Myosin I can act as a molecular
653 force sensor. *Science*. 321:133–6. doi:10.1126/science.1159419.
654 Laakso, J.M., J.H. Lewis, H. Shuman, and E.M. Ostap. 2010. Control of myosin-I force sensing
655 by alternative splicing. *Proc. Natl. Acad. Sci. U. S. A.* 107:698–702.
656 doi:10.1073/pnas.0911426107.
657 Lewellyn, E.B., R.T. Pedersen, J. Hong, R. Lu, H.M. Morrison, and D.G. Drubin. 2015. An
658 Engineered Minimal WASP-Myosin Fusion Protein Reveals Essential Functions for
659 Endocytosis. *Dev. Cell*. 35:281–294. doi:10.1016/j.devcel.2015.10.007.
660 Lewis, J.H., T. Lin, D.E. Hokanson, and E.M. Ostap. 2006. Temperature dependence of
661 nucleotide association and kinetic characterization of Myo1b. *Biochemistry*. 45:11589–
662 97. doi:10.1021/bi0611917.
663 Lin, T., N. Tang, and E.M. Ostap. 2005. Biochemical and motile properties of Myo1b splice

664 isoforms. *J. Biol. Chem.* 280:41562–41567. doi:10.1074/jbc.M508653200.

665 Manenschijn, H.E., A. Picco, M. Mund, J. Ries, and M. Kaksonen. 2019. Type-I myosins
666 promote actin polymerization to drive membrane bending in endocytosis. *Elife*.
667 17:490011. doi:10.1101/490011.

668 El Mezgueldi, M., N. Tang, S.S. Rosenfeld, and E.M. Ostap. 2002. The Kinetic Mechanism of
669 Myo1e (Human Myosin-IC). *J. Biol. Chem.* 277. doi:10.1074/jbc.M200713200.

670 Mogilner, A., and G. Oster. 1996. Cell motility driven by actin polymerization. *Biophys. J.*
671 71:3030–3045. doi:10.1016/S0006-3495(96)79496-1.

672 Mogilner, A., and G. Oster. 2003. Force Generation by Actin Polymerization II: The Elastic
673 Ratchet and Tethered Filaments. *Biophys. J.* 84:1591–1605. doi:10.1016/S0006-
674 3495(03)74969-8.

675 Mund, M., J.A. Van Der Beek, J. Deschamps, S. Dmitrieff, P. Hoess, J.L. Monster, A. Picco, F.
676 Nedelec, M. Kaksonen, and J. Ries. 2018. Systematic Nanoscale Analysis of Endocytosis
677 Links Efficient Vesicle Formation to Patterned Actin Nucleation. *Cell*. 174:884–896.
678 doi:10.1016/j.cell.2018.06.032.

679 Nickaeen, M., J. Berro, T.D. Pollard, and B.M. Slepchenko. 2019. Actin assembly produces
680 sufficient forces for endocytosis in yeast. *Mol. Biol. Cell*. 30:2014–2024.
681 doi:10.1091/mbc.E19-01-0059.

682 Pedersen, R.T., and D.G. Drubin. 2019. Type I myosins anchor actin assembly to the plasma
683 membrane during clathrin-mediated endocytosis. *J. Cell Biol.* 218:1138–1147.
684 doi:10.1083/jcb.201810005.

685 Picco, A., M. Mund, J. Ries, F. Nedelec, and M. Kaksonen. 2015. Visualizing the functional
686 architecture of the endocytic machinery. *Elife*. 4:1–29. doi:10.7554/eLife.04535.

687 Pyrpassopoulos, S., G. Arpağ, E.A. Feeser, H. Shuman, E. Tüzel, and E.M. Ostap. 2016. Force
688 generation by membrane-associated myosin-I. *Sci. Rep.* 6:1–14.
689 doi:10.1038/srep25524.
690 Roy, M.A., N. Siddiqui, and D. D'Amours. 2011. Dynamic and selective DNA-binding activity
691 of Smc5, a core component of the Smc5-Smc6 complex. *Cell Cycle*. 10:690–700.
692 doi:10.4161/cc.10.4.14860.
693 Skruzny, M., T. Brach, R. Ciuffa, S. Rybina, M. Wachsmuth, and M. Kaksonen. 2012.
694 Molecular basis for coupling the plasma membrane to the actin cytoskeleton during
695 clathrin-mediated endocytosis. *Proc. Natl. Acad. Sci. U. S. A.* 109:E2533–E2542.
696 doi:10.1073/pnas.1207011109.
697 Snoberger, A., B. Barua, J.L. Atherton, H. Shuman, E. Forgacs, Y.E. Goldman, D.A.
698 Winkelmann, and E.M. Ostap. 2021. Myosin with hypertrophic cardiac mutation r712l
699 has a decreased working stroke which is rescued by omecamtiv mecarbil. *Elife*. 10:1–
700 24. doi:10.7554/eLife.63691.
701 Sokac, A.M., C. Schietroma, C.B. Gundersen, and W.M. Bement. 2006. Myosin-1c couples
702 assembling actin to membranes to drive compensatory endocytosis. *Dev. Cell*. 11:629–
703 40. doi:10.1016/j.devcel.2006.09.002.
704 Spudich, J.A., and S. Watt. 1971. The Regulation of Rabbit Skeletal Muscle Contraction. *J.*
705 *Biol. Chem.* 246:4866–4871.
706 Stewart, T.J., V. Murthy, S.P. Dugan, and J.E. Baker. 2021. Velocity of myosin-based actin
707 sliding depends on attachment and detachment kinetics and reaches a maximum when
708 myosin-binding sites on actin saturate. *J. Biol. Chem.* 297.
709 doi:10.1016/j.jbc.2021.101178.

710 Sun, Y., A.C. Martin, and D.G. Drubin. 2006. Endocytic Internalization in Budding Yeast
711 Requires Coordinated Actin Nucleation and Myosin Motor Activity. *Dev. Cell*. 11:33–46.
712 doi:10.1016/j.devcel.2006.05.008.
713 Sun, Y., J. Schöneberg, X. Chen, T. Jiang, C. Kaplan, K. Xu, T.D. Pollard, and D.G. Drubin. 2019.
714 Direct comparison of clathrin-mediated endocytosis in budding and fission yeast
715 reveals conserved and evolvable features. *Elife*. 8. doi:10.7554/eLife.50749.
716 Takagi, Y., E.E. Homsher, Y.E. Goldman, and H. Shuman. 2006. Force generation in single
717 conventional actomyosin complexes under high dynamic load. *Biophys. J.* 90:1295–
718 1307. doi:10.1529/biophysj.105.068429.
719 Veigel, C., L.M. Coluccio, J.D. Jontes, J.C. Sparrow, R. a Milligan, and J.E. Molloy. 1999. The
720 motor protein myosin-I produces its working stroke in two steps. *Nature*. 398:530–
721 533. doi:10.1038/19104.
722 Woody, M.S., M.J. Greenberg, B. Barua, D.A. Winkelmann, Y.E. Goldman, and E.M. Ostap.
723 2018. Positive cardiac inotrope omecamtiv mecarbil activates muscle despite
724 suppressing the myosin working stroke. *Nat. Commun.* 9. doi:10.1038/s41467-018-
725 06193-2.
726 Woody, M.S., J.H. Lewis, M.J. Greenberg, Y.E. Goldman, and E.M. Ostap. 2016. MEMLET: An
727 Easy-to-Use Tool for Data Fitting and Model Comparison Using Maximum-Likelihood
728 Estimation. *Biophys. J.* 111:273–282. doi:10.1016/j.bpj.2016.06.019.
729 Woody, M.S., E.M. Ostap, Y.E. Goldman, and M. Capitanio. 2017. An ultra-fast EOD-based
730 force-clamp detects rapid biomechanical transitions. SPIE-Intl Soc Optical Eng. 26.
731

Figure 1: Models for the functions of actin assembly and myosin activity during membrane deformation for clathrin-mediated endocytosis

Cartoon diagram illustrating the organization of actin filaments and Myo5 molecules at endocytic sites. Actin filaments are bound by coat proteins at the tip of the growing membrane invagination and oriented with their growing ends toward the plasma membrane, powering membrane invagination. The type I myosin Myo5 could either anchor the actin network in a favorable orientation (left) or provide an assisting force (right).

Figure 2: In-solution, population biochemical characterization of Myo5

(A) Coomassie-stained SDS-polyacrylamide gels showing example preparations of the purified Myo5 motor/lever construct and calmodulin (Cmd1, light chain) used in all experiments. **(B)** The actin concentration dependence of the steady-state ATPase activity of 100 nM unphosphorylated (grey circles) and phosphorylated Myo5 (black circles). Each data point represents the average of 6-7 time courses, which were 100 s each. The orange line is a best fit of the phosphorylated Myo5 data to a rectangular hyperbola. **(C)** Schematic pathway for the Myo5 ATPase cycle. Blue motors are in tightly bound conformations, green motors are weakly bound/unbound. **(D)** Example light scattering transients reporting on ATP-induced dissociation of phosphorylated (left, k_{obs} = 17 s^{-1}) and unphosphorylated (right, k_{obs} = 64.1 s^{-1}) actoMyo5, obtained by mixing 100 nM actoMyo5 (AM) with 94 μm and 72 μM ATP, respectively, as shown in the inset schematic. The black line is the fit of a single exponential function to the data. **(E)** ATP concentration dependence of dissociation of 100 nM unphosphorylated (grey circles) and phosphorylated actoMyo5 (black circles). Each data point represents 3-6 time courses averaged and fit to a single exponential decay

function. The orange line is a linear best fit of the phosphorylated Myo5 data. The purple line is a best fit of the unphosphorylated Myo5 data to a rectangular hyperbola. **(F)** Example light scattering transients reporting ATP-induced dissociation of ADP-saturated phosphorylated (left) and unphosphorylated (right) actoMyo5, obtained by preincubating 200 nM actoMyo5 (AM) with 100 μM ADP, then mixing rapidly with 2.5 mM ATP, as shown in the inset schematic. The black line is the fit of a single exponential function to the data. **(G)** Velocity of actin filament gliding, measured at varying surface densities of Phospho-Myo5 (black circles, orange line) and unphosphorylated Myo5 (gray circles, purple line) in in vitro motility assays. Myosin concentrations indicate the quantity of protein incubated in the flow chamber before washing. Each data point represents the average velocity of 30 – 60 filaments, and the error bars are standard deviations.

Table 1

Summary of rate and equilibrium constants measured for Myo5 in this study. Errors are standard errors of the fits.

Figure 3: Single molecule, optical trap analysis of Myo5 step size and kinetics

(A) Cartoon schematic of the 3-bead optical trapping setup. A biotinylated actin filament is tethered between two neutravidin-coated beads that are trapped in a dual beam optical trap. This bead-actin-bead "dumbbell" is lowered onto pedestal beads that have been sparsely coated with His_6 antibody to attach Myo5-motor/lever-Avi-Tev-His_9. **(B-D)** Single Myo5 displacements of a single bead position and covariance traces, calculated using both beads, showing single molecule interactions acquired in the presence of 1 μM **(B)** 10 μM

778 **(C)** and 1000 μM ATP. **(D)**. Blue bars indicate attachment events as identified by covariance
779 (gray) decreases. The threshold of event detection by the covariance traces are indicated
780 by dashed gray lines. **(E)** Schematic of displacement traces depicting the 2-step nature of
781 actomyosin displacements in the optical trap. **(F-H)** Binding events were synchronized at
782 their beginnings (left) or ends (right) and averaged forward or backward in time,
783 respectively. Measured total displacement of Myo5 was 5.0 nm at 10 μM ATP, with the 1st
784 substep contributing a 4.8 nm displacement (arrow 1. in G) and the 2nd substep
785 contributing a 0.2 nm displacement (arrow 2. In G). **(F-H, left)** Forward-averaged
786 ensembles synchronized at the beginnings of events. **(F-H, right)** Reverse-averaged
787 ensembles synchronized at the ends of events. Black and gray lines are single exponential
788 fits in the forward and reverse ensembles, respectively. **(I)** Cumulative distributions of
789 attachment durations for Myo5 at 1, 10, and 1000 μM ATP. Blue lines show cumulative
790 frequency of attachment durations at the indicated ATP concentrations, and the red,
791 yellow, and green lines indicate fitted exponential distributions at 1, 10, and 1000 μM ATP,
792 respectively. 1 and 10 μM ATP were fit well to single exponentials, and the 1000 μM ATP
793 data were best described by the sum of two exponentials. **(J)** Summary of rates at 1, 10, and
794 1000 μM ATP calculated from (F-H). Blue boxes are the fitted exponential distributions
795 from (I), black diamonds are forward ensemble fits from (F-H, left), and gray diamonds are
796 reverse ensemble fits from (F-H, right). At lower concentrations of ATP (1 and 10 μM), the
797 rate of detachment is limited by ATP association, corresponding to the reverse ensemble
798 fits, while at saturating ATP concentration (1000 μM), the detachment rate is limited by the
799 rate of ADP dissociation, corresponding to the forward ensemble fits. **(K)** Summary of rates
800 determined via single molecule optical trapping. Errors for detachment rates are 95%

801 confidence intervals. Errors for forward and reverse ensemble fits are standard errors of
802 the fits. *Detachment rates at 1000 μM ATP were best fit to the sum of 2 exponents. The
803 major component of the fit (67.8 s^{-1}) comprises 92.1% of the total with the remaining 7.9%
804 having a rate of 11.6 s^{-1}.
805
806 **Figure 4: Myo5 attachment lifetimes are substantially less force-dependent than**
807 **other known type I myosins**
808 An isometric optical force clamp was utilized to determine the force-sensitivity of the
809 detachment of Myo5 from actin. **(A)** Durations of individual actomyosin attachments as a
810 function of force, plotted on a semi-log scale **(B)** The solid black line shows the force
811 dependence of the detachment rates determined by MLE fitting of unaveraged points in A.
812 For illustration purposes, attachment durations from (A) were binned by force at every 10
813 points, averaged, and converted to rates. Best- fit parameters were determined by MLE
814 fitting and 95% confidence intervals were calculated via bootstrapping. The solid black line
815 is calculated from best fit parameters (k = 67.6 s^{-1}, d = 1.14 nm), while the gray shaded
816 region is the 95% confidence interval (k = 62.4-72.9 s^{-1}, d = 1.03-1.26 nm). All MLE fitting
817 was performed on unaveraged data and was corrected for instrument deadtime. **(C)** The
818 force dependent detachment rate of Myo5 (from panel B) plotted alongside the force
819 dependent detachment rates for Myo1b, Myo1c, and β-cardiac muscle myosin, Myh7. **(D)**
820 Power output for the same four myosins calculated over a range of forces by multiplying
821 the functions from (C) by the applied force F, and the step size and duty ratios of each
822 myosin.
823

Figure S1: P21 Activated Kinase 1 (Pak1) phosphorylates Myo5 on S357

Crude preparations of wild type and S357A Myo5 motor/lever constructs were mixed with 250 μM ATP including 20 μCi of ATPγP32 in kinase assay buffer (5 mM MOPS pH 7, 2.5 mM β-glycerophosphate, 5 mM $MgCl_2$, 400 μM EDTA, 1 mM EGTA, 50 μM DTT) in either the presence or absence of Pak1. Reactions were incubated at 25˚C for 60 minutes, then quenched by adding an equal volume of 2x tris urea sample buffer (125 mM Tris pH 6.8, 6 M urea, 2% SDS, 0.1% bromophenol blue, 10% β-mercaptoethanol) and resolved on a 10% polyacrylamide gel. The gel was stained with Coomassie, then dried onto Whatman paper and exposed to a storage phosphor screen (Amersham). The Coomassie-stained gel was imaged on a standard photo scanner and the phosphor screen on a Typhoon gel imager (Amersham). Note that there are differences in baseline labeling in the absence of added kinase between the two different protein preps, but addition of Pak1 clearly results in radiolabeling of wild type but not mutant Myo5.

Movie S1: Motility assays with phosphorylated Myo5

Rhodamine phalloidin-labeled actin filaments gliding over coverslips coated with a concentration series of phosphorylated Myo5 protein in motility buffer with 1 mM ATP. Movies were collected at 1 frame per second and are played back at 16 frames per second.

Movie S2: Motility assays with unphosphorylated Myo5

Rhodamine phalloidin-labeled actin filaments gliding over coverslips coated with a concentration series of unphosphorylated Myo5 protein in motility buffer with 1 mM ATP.

847 Short movies of motility at 100 nM and 150 nM unphosphorylated Myo5 were collected
848 because no motility was observed. Movies at all other concentrations were collected at 1
849 frame every 4 seconds and are played back at 16 frames per second. The playback rate of
850 Movie S2 is four times faster than the playback rate of Movie S1.

Figure 1

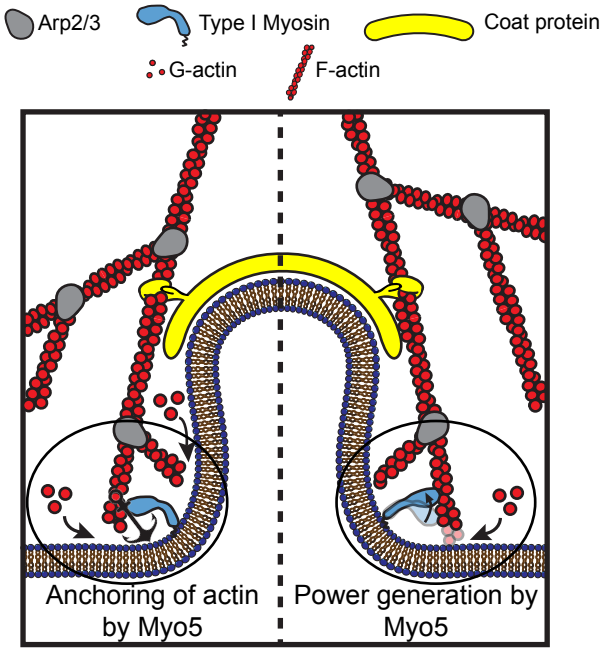

Figure 2

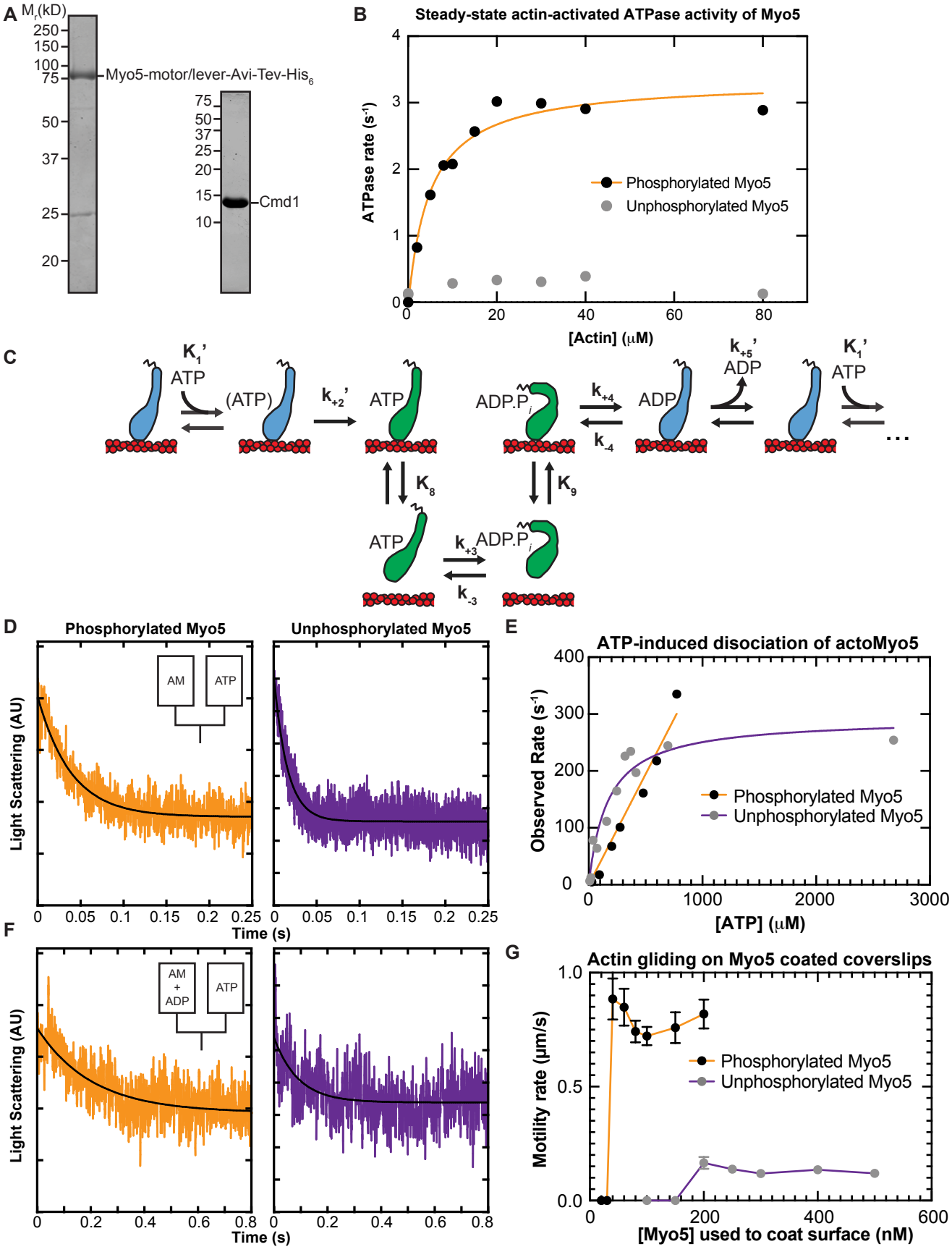

Table 1: Rate and equilibrium constants of the Myo5 ATPase cycle

	Phosphorylated Myo5	**Unphosphorylated Myo5**
Steady-state actin-activated ATPase		
V_{max} (s^{-1})	3.3 (± 0.15)	ND
K_{ATPase} (μM)	5.1 (± 0.88)	ND
ATP binding		
K_1' (μM^{-1})	ND	0.006 (± 0.0016)
k_{+2}' (s^{-1})	≥ 335	290 (± 24)
$K_1'k_{+2}'$ ($\mu M^{-1}\ s^{-1}$)[a]	0.39 (± 0.017)[b]	1.1 (± 0.28)[c]
ADP release		
k_{+5}' (s^{-1})	74 (± 2.0)	107 (± 5.9)

[a]Determined from a linear fit of the unbinding rates. [b]Linear fit of all data for Phosphorylated Myo5 in Fig. 2E. [c]Linear fit of observed rates below 100 μM ATP for Unphosphorylated Myo5 in Fig 2E. ND: Not Determined.

Figure 3

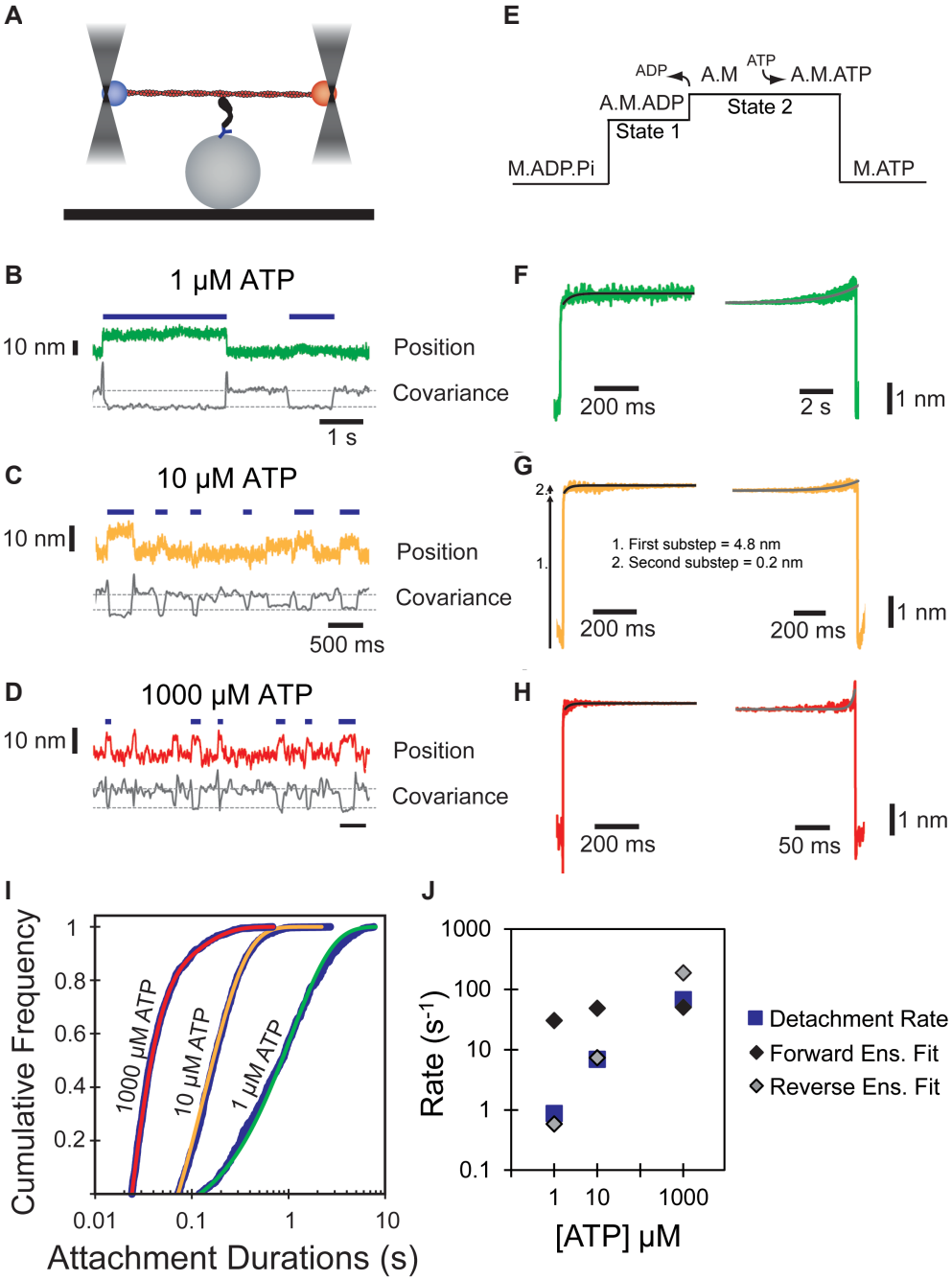

K

Summary of rates determined during single molecule optial trapping

[ATP] μM	Detachment Rate (s^{-1})	Forward Ensemble Fit (s^{-1})	Reverse Ensemble Fit (s^{-1})
1	0.88 (+/- 0.07/0.07)	>30	0.59 (+/- 0.003)
10	6.9 (+/- 0.49/0.46)	49 (+/- 1.6)	7.3 (+/- 0.1)
1000	67.8* (+/- 11.9/8.7)	50 (+/- 0.2)	>187

Figure 4